GeoScienceWorld
Lithosphere
Volume 2022, Article ID 4061650, 12 pages
https://doi.org/10.2113/2022/4061650

Lithosphere

Research Article

Passive Tomographic Study on Velocity Changes in Underground Mines Using Tabular Mesh Grids

Xu Ma,[1,2] **Erik Westman**,[2] **Kai Guo**,[3] **Enji Sun**,[4] **and Tao Yang**[5]

[1]*Division State Key Laboratory of Earthquake Dynamics, Institute of Geology, China Earthquake Administration, Beijing, China*
[2]*Department of Mining and Minerals Engineering, Virginia Tech, Blacksburg, VA 24060, USA*
[3]*China Earthquake Networks Center, Beijing 100045, China*
[4]*China Academy of Safety Science and Technology, Beijing 100012, China*
[5]*North China Institute of Science and Technology, Hebei 06521, China*

Correspondence should be addressed to Tao Yang; yangtao585@163.com

Received 28 March 2022; Accepted 8 July 2022; Published 16 August 2022

Academic Editor: Wenzhuo Cao

Double difference tomographic inversion on measurements of travelling time and location are performed to analyze the velocity structure within rock mass in underground mining. Residuals of each iteration are estimated to evaluate the conversion of computation. Average wave propagation velocities in tabular areas are assessed to compare the velocity change affected by mainshocks. It is summarized that velocity increases before mainshocks and then reduces with temporal evolution after them. Possible explanations include static stress buildup that enhances the wave propagation before mainshocks and static stress reduction that weakens the waveform propagation. Additionally, wave propagation is attenuated by the dynamic-shaking induced fractures and ruptures within rock masses. Velocity change is shown to be of importance in assessing the stress redistribution and stability of rock masses. It is found that P-wave velocity increased by 1%~5% before the occurrence of mainshocks. After the mainshocks, the velocity turned into decreasing and eventually dropped to a level that was even lower than the average level before the mainshocks. It can be inferred that stress increased and formed a stress concentration region before the mainshocks. The occurrence of mainshocks caused damage and stress relaxation in the rock mass, leading to a significant velocity decrease.

1. Introduction

Passive tomographic model is widely used to characterize the structure of earth crust by minimizing difference between simulated and observed seismic waveforms [1, 2]. Iterative inversions on both locations of seismic events and the velocity structure are performed till achieving the minimal error [3, 4]. Analyses of velocity change associated with earthquakes provide evidence that velocity tends to significantly decrease after earthquakes [5]. It is revealed that P- and S-wave velocities decrease with damaged rock in the earthquakes and velocity recovered due to the healing effect [6–8]. Seismic imaging and microseismic monitoring are used to detect highly stressed and failed regions of underground mines, especially in hard rock mines [9–14].

In Situ stress redistribution influenced by mining excavation can be analyzed by numerical modeling, InSar monitoring, and seismic monitoring in association with tomography to show velocity anomalies [15, 16]. Studies suggested that reliable microseismic monitoring systems are playing a key role for mining safety [17–19]. The ability of forecasting mainshocks in mine management is crucial for establishing and effectively employing a protocol for seismic hazards mitigation [20]. However, completing the knowledge of how to forecast rock bursts using microseismic events still needs more investigation [21]. It is found that velocity structure of rock masses can reveal the fracture-induced anisotropy and burst-prone regions in mining [10, 14, 22, 23].

The aim of this paper is to investigate the velocity change affected by the occurrence of mainshocks (Mn>1) in underground mining. A three-dimensional tomographic model of

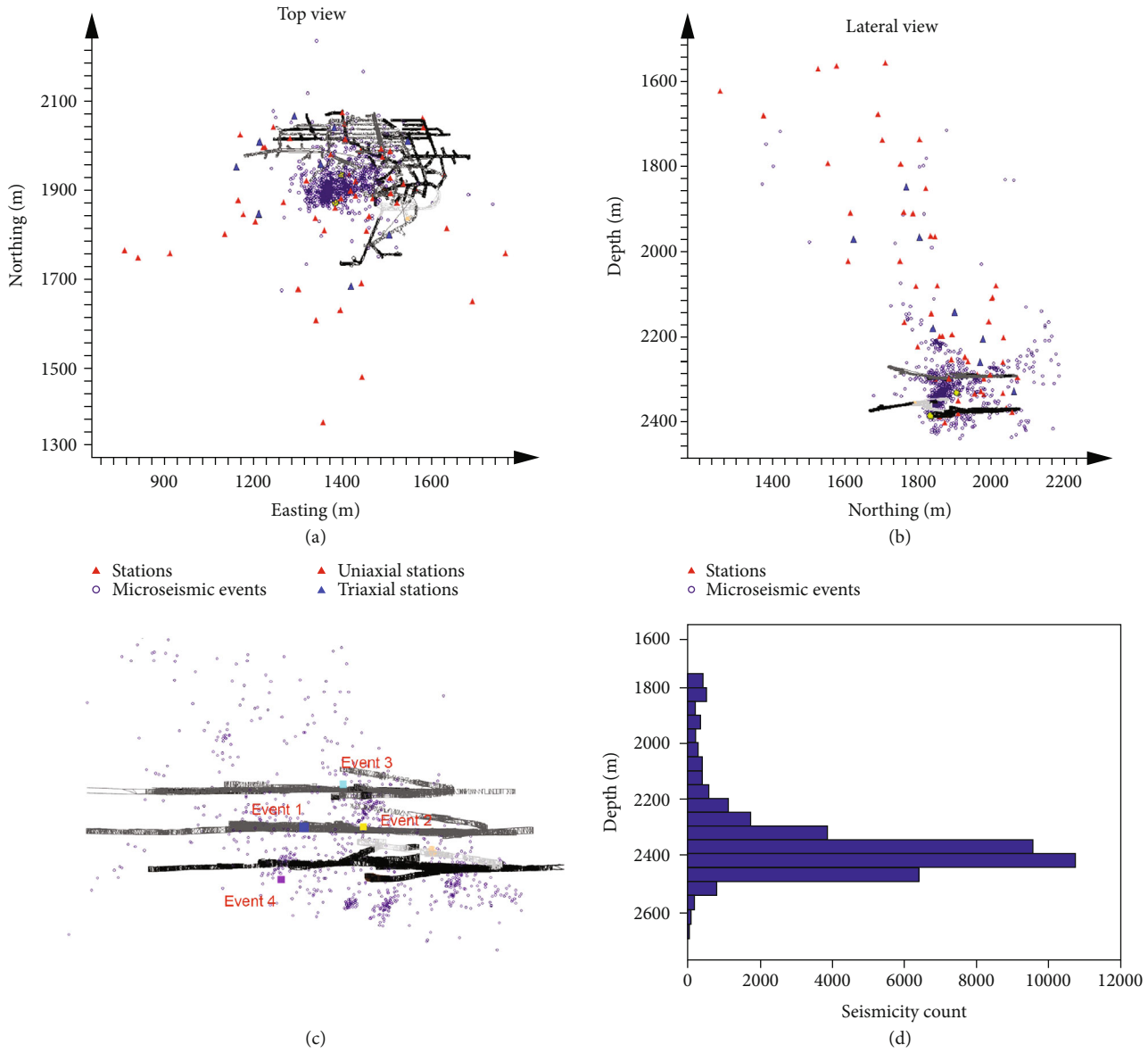

Figure 1: The seismic monitoring system and production drifts of Creighton Mine in (a) top view and (b) lateral view. (c) The spatial distribution of mainshocks and (d) the depth range of microseismic events of Creighton Mine.

the mining region is established to display the velocity change due to the occurrence of mainshocks.

2. Data and Methods

2.1. Site Description. Two underground mines, Creighton Mine and Kidd Mine, are investigated in this study and they have been seismically active due to the great depths of mining operations in hard-rock metal mines. Both mines are installed with high resolution seismic monitoring systems provided by ESG Solutions. Both seismic monitoring systems consist of a microseismic monitoring system and a strong ground motion system. Stations of the microseismic monitoring system are installed in subsurface. The microseismic monitoring system is mainly responsible for monitoring and recording microseismicity. In contrast, the strong ground motion system is installed on the surface above the ground and is used for monitoring seismic events with higher magnitude (>1.0), which are also called major events.

In Creighton Mine, the extraction rate is nearly 2200 tons per day and the deepest operations are around a depth of 2500 m. A variety of mining methods including blastholes, cut-and-fill, and vertical retreat mining have been used in the upper region of Creighton Mine. The large-diameter blasthole method is currently used in depth from 1800 to 2500 m. The microseismic monitoring system of the local seismic network includes 10 triaxial stations and 52 uniaxial stations. Figures 1(a) and 1(b) show the location of stations of the microseismic monitoring system, which provides a good coverage of the microseismic events.

The operations of Kidd Mine are around 2930 m below the earth's surface and Kidd Mine uses the blasthole

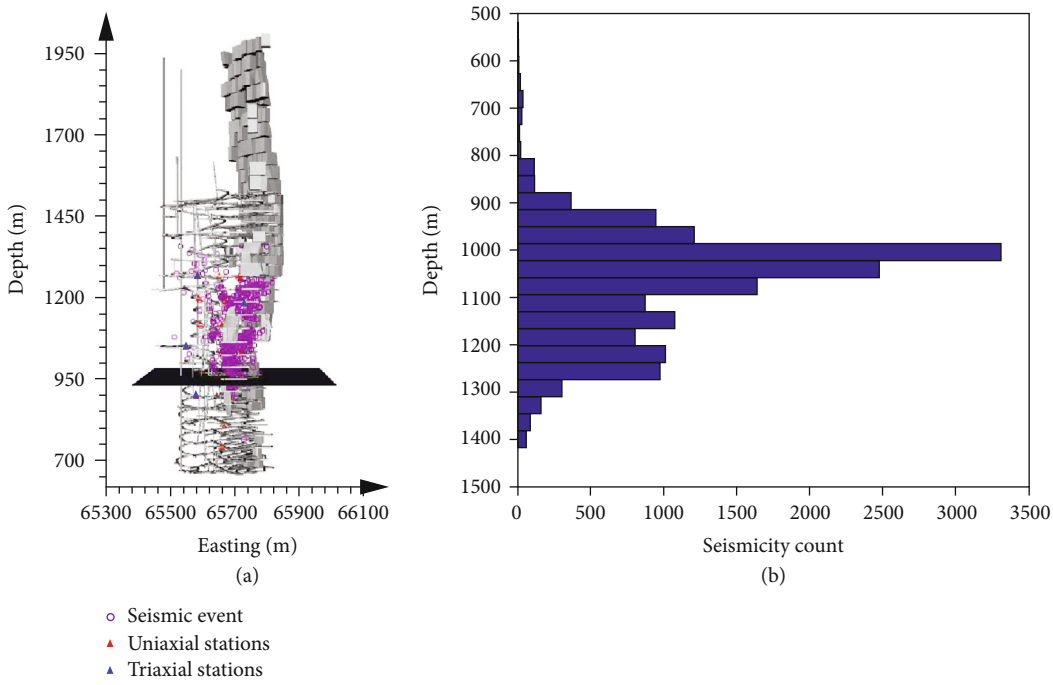

Figure 2: (a) The distribution of stations and seismic events of Kidd Mine. (b) The depth range of seismic events of Kidd Mine.

Table 1: Times, Locations, and Magnitude of mainshocks in Creighton Mine.

Events	Time	North (m)	East (m)	Depth (m)	Magnitude
1	7/6/2011 8 : 41	1927	1399	2333	3.1
2	7/6/2011 8 : 46	1915	1478	2332	1.2
3	7/6/2011 8 : 47	1885	1458	2284	1.3
4	7/10/2011 2 : 44	1861	1383	2391	1.4

stopping with cement backfill mining method. More than 7000 tons per day are produced in Kidd Mine. Three ore types including massive, banded, and bedded ores are found in the orebody of Kidd Mine. The microseismic monitoring system in Kidd Mine includes 8 triaxial stations and 23 uniaxial stations (Figure 2(a)).

2.2. Mainshocks and Microseismic Events. In the underground mines, seismic stations of microseismic monitoring systems are installed at a great depth to ensure accurate monitoring of microseismic events. Referring to the record of seismic events in the data set of Creighton Mine, a considerable number of seismic events occurred from April, 2011 to March, 2012. It exhibits that the seismic events at the depth of 7000 – 8000 ft take up over 90% of all the seismic events (Figure 1(d)). Creighton Mine experienced four mainshocks in July, 2011 (Table 1). The location of microseismic events and mainshocks provided the reference to the dimension and spatial location for the velocity model.

Velocity distribution prior to mainshocks and redistribution following them are compared to discuss the velocity change affected by mainshocks. The seismic network of Creighton Mine provides a good quality seismic dataset for high resolution tomographic inversion. Velocity profile within a certain spatial and temporal scale is accomplished based on waveform propagation from seismicity to receivers. The period from July 6th to July 10th, 2011 is emphasized because the knowledge on whether some pronounced changes exhibit around the occurrences of four mainshocks would benefit seismic hazard assessment in underground mines. The long-term and short-term temporal distribution of Creighton Mine is shown in Figure 3(a).

Seismic events are picked and compiled to groups of event-receiver pairs based on whether they occurred prior to or after the mainshocks. Velocity inversion results are compared to evaluate the change between velocity distributions before and after mainshocks. Each group includes 2000 events. Events in all groups are arranged sequentially in time. A double difference tomography method is used to invert simultaneously the location of seismicity and distribution of velocity. The comprehensive description of the tomographic method and software package manual is given by Zhang [3, 4].

Unlike all mainshocks of Creighton Mine occurring within a short period range, the two mainshocks in Kidd Mine were induced in January and June. As a result of two

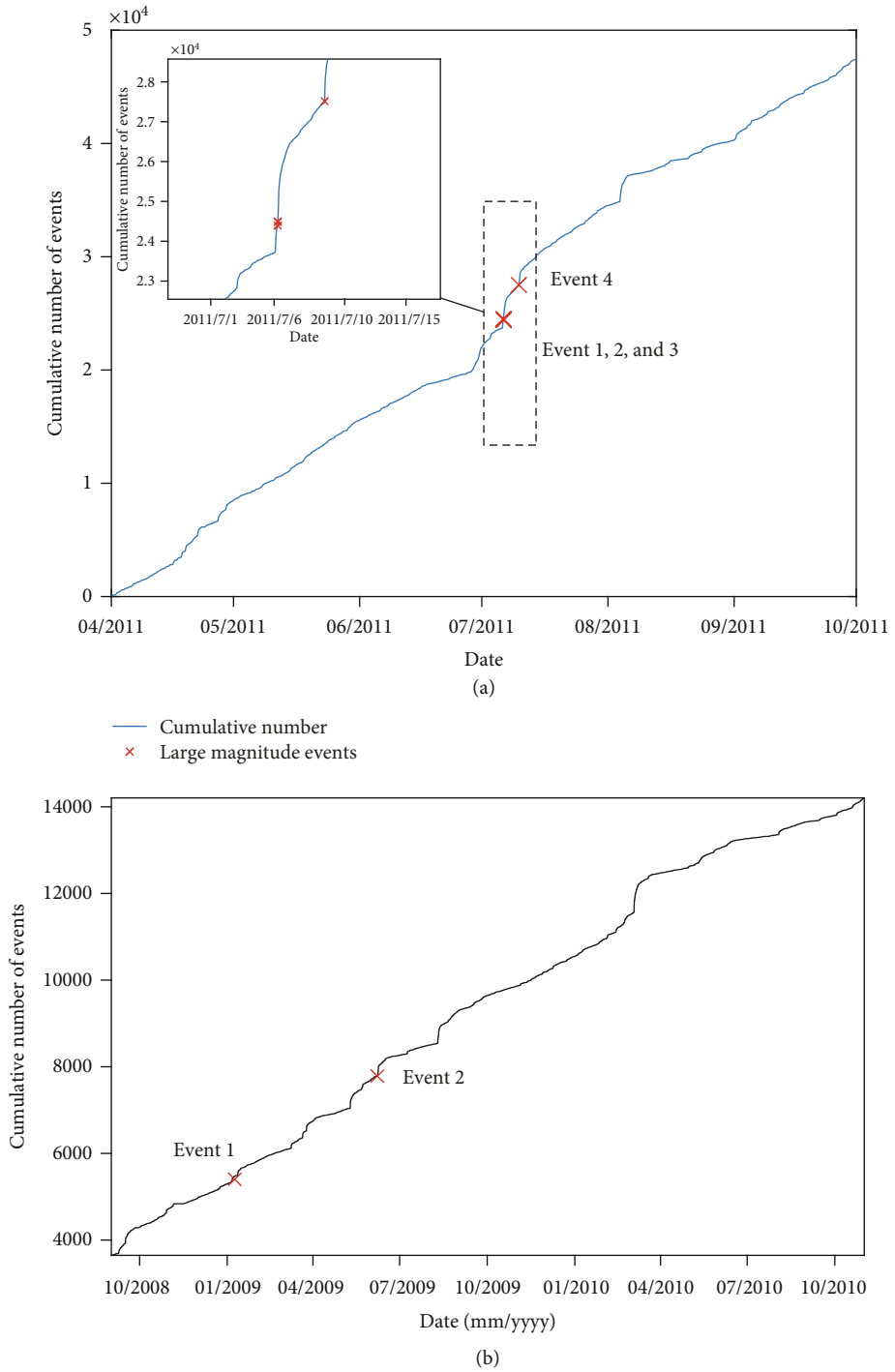

Figure 3: Cumulative number of events in temporal distribution and mainshocks distribution of (a) Creighton Mine and (b) Kidd Mine.

Table 2: Events Grouped for tomographic studies in Creighton Mine.

Group	From	To	Number of events
First group before mainshocks	6/29/2011 6 : 23 : 17	7/1/2011 16 : 58 : 54	2000
Second group before mainshocks	7/1/2011 17 : 18 : 11	7/6/2011 8 : 40 : 32	2000
First group after mainshocks	7/10/2011 2 : 44 : 58	7/12/2011 2 : 58 : 59	2000
Second group after mainshocks	7/12/2011 21 : 08 : 51	7/19/2011 16 : 11 : 40	2000

Table 3: Events grouped for tomographic studies in Kidd Mine.

Events Groups	From	To	Number of Events
First group before mainshock 1	10/07/2008 19:20:20	11/20/2008 04:23:44	500
Second group before mainshock 1	11/20/2008 05:56:53	01/06/2009 04:07:31	500
First group after mainshock 1	01/06/2009 04:57:40	02/05/2009 09:06:37	500
Second group after mainshock 1	02/05/2009 15:06:36	03/21/2009 03:50:20	500
First group before mainshock 2	05/10/2009 05:58:16	05/28/2009 16:44:05	500
Second group before mainshock 2	05/28/2009 21:18:27	06/15/2009 17:40:13	500
First group after mainshock 2	06/15/2009 19:19:49	08/10/2009 06:46:51	500
Second group after mainshock 2	08/10/2009 06:57:17	08/24/2009 16:53:46	500

Table 4: Times, locations, and magnitude of mainshocks in Kidd Mine.

Events	Date	Time	North (m)	East (m)	Depth (m)	Magnitude
1	January, 6th 2009	4 : 40 AM	65733	65686	1150	3.8
2	June, 15th 2009	7 : 01 PM	65861	65737	1035	3.1

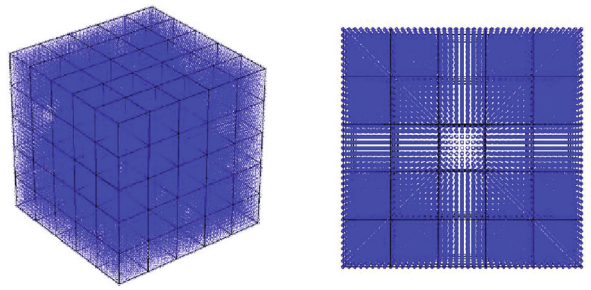

Figure 4: Mesh grids ($40 \times 40 \times 40$) of velocity model in (a) isometric view and (b) top view. The tomographic imaging is unified and shown in the delineated cube ($5 \times 5 \times 5$).

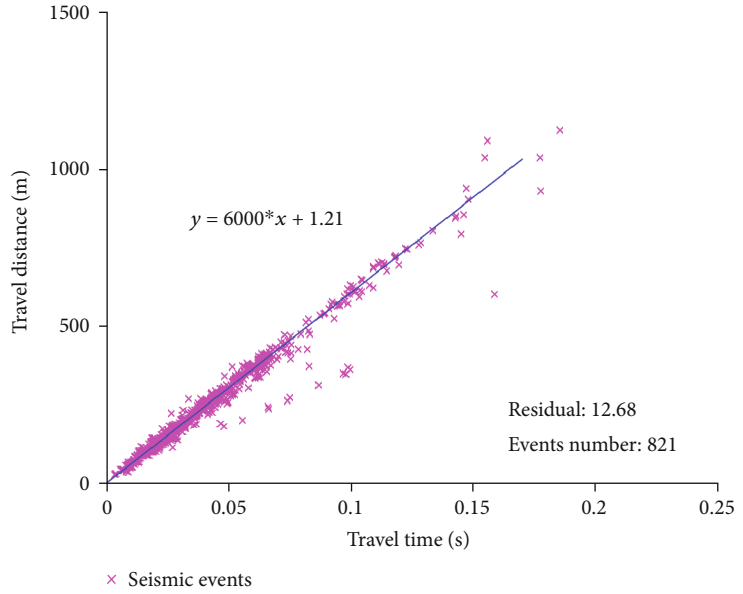

Figure 5: Linear regression of P-wave travel times versus travel distances from seismic events to stations in Creighton Mine. The slope of the blue line represents the average velocity of raypaths. The slope of the linear fitting line is used as the initial P-wave velocity, which is applied to grid nodes of velocity models (Figure 4) for the initial inversion.

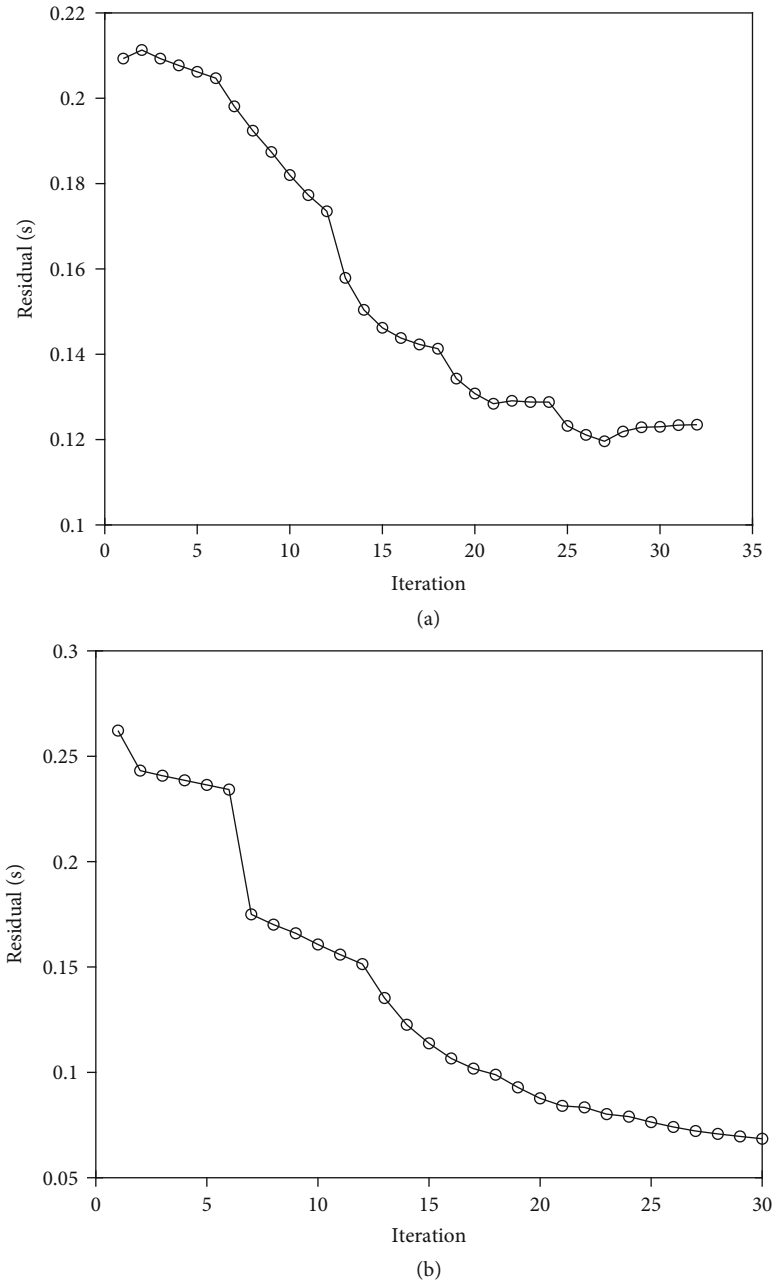

Figure 6: The examples of monitoring residual with iterations of velocity inversion of (a) Creighton Mine and (b) Kidd Mine.

different periods including mainshocks, 2000 events are split into four groups. Each group of Creighton Mine consists of 2000 microseismic events (Table 2), while 500 events are included in each group of Kidd Mine (Table 3). Two main factors are considered to determine the number of events in each group. First, the events could provide enough raypaths traveling through the target areas. Then, periods based on the choice of the number of events should be in reasonable ranges in this tomographic study. Monitoring of seismicity at Kidd Mine shows that two mainshocks occurred, respectively, in January and June, 2009 (Table 4). As shown in Figure 3(b) for temporal distribution of mainshocks, the occurrence of mainshocks is correlated with a significant increase of cumulative number of microseismic events within a short period of time. The number of events distributions on corresponding depth is shown in Figure 2.

2.3. Average Velocity Analysis in Tabular Areas. It has been proved that the velocity of wave propagation in rock masses is correlated with the effective stresses [14, 24, 25]. Stress distribution significantly affects the P-wave velocity travelling in rocks. The quantitative relationship between these elements is summarized as

$$V_p = \sqrt{\frac{K + 4/3\mu}{\rho}} \quad (1)$$

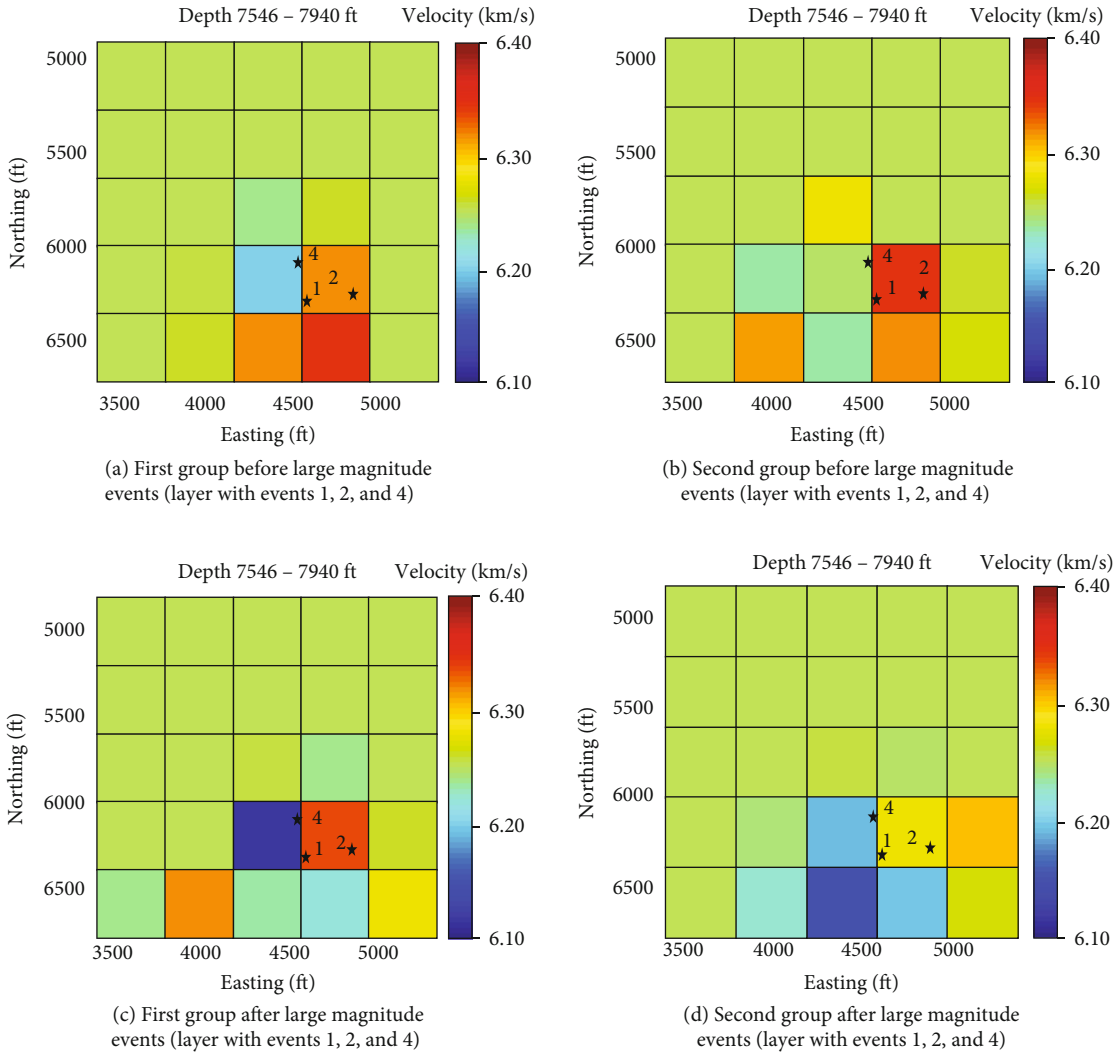

(a) First group before large magnitude events (layer with events 1, 2, and 4)

(b) Second group before large magnitude events (layer with events 1, 2, and 4)

(c) First group after large magnitude events (layer with events 1, 2, and 4)

(d) Second group after large magnitude events (layer with events 1, 2, and 4)

FIGURE 7: Temporal velocity evolution with mainshock 1, 2, and 4 of Creighton Mine in depth range 2300-2420 m: (a) the first group (June 29 – July 1) before mainshocks; (b) the second group (July 1 – July 6) before mainshocks; (c) the first group (July 10 – July 12) after mainshocks; (d) the second group (July 12 – July 19) after mainshocks.

where V_P is the P-wave velocity, ρ is the density of rock, K is the bulk modulus, and μ is the shear modulus [25].

We used a double-difference package tomoDD [3, 4], which was developed based on a series of double-difference algorithms including hypoDD [26]. This double-difference tomographic tool implements the velocity inversion along with relocating seismic events to obtain the optimal velocity structures [27]. The double-difference residual is quantified by extracting the catalog of arrival time,

$$dr_k^{ij} = \left(t_k^i - t_k^j\right)^{obs} - \left(t_k^i - t_k^j\right)^{cal} \quad (2)$$

where $\left(t_k^i - t_k^j\right)^{obs}$ is the difference of the observed arrival times between events i and j, and $\left(t_k^i - t_k^j\right)^{cal}$ is the difference of the computed arrival times between events i and j.

To analyze the influence on velocity posted by mainshocks, velocity results computed by double difference tomography are visualized in tabular areas. tomoDD is used to perform velocity inversion on 3D nodes, which consists of $40 \times 40 \times 40$ nodes (Figure 4). All nodes are assigned with a same initial velocity value (Creighton Mine 6000 m/s; Kidd Mine 6025 m/s). The initial velocities are estimated by linear fit on travel time and travel distance of raypaths traveling through the rock mass. As shown in Figure 5, linear regression was performed for Creighton Mine to determine the optimal value of initial velocity assigned for the velocity model. In the same manner, linear regression is performed for Kidd Mine based on the travel distance and travel time. Velocity inversion is performed at each node. All nodes are divided by $5 \times 5 \times 5$ mesh grids cubes, as shown in Figure 4. Average velocity of each unit cube is computed by all the velocity of nodes in the same unit cube. This velocity model is developed to spatially cover the mainshocks so that abundant raypaths travel through the velocity model, ensuring the resolution of velocity inversion.

The accuracy of tomographic studies for seismic events was determined by the density of raypaths traveling through

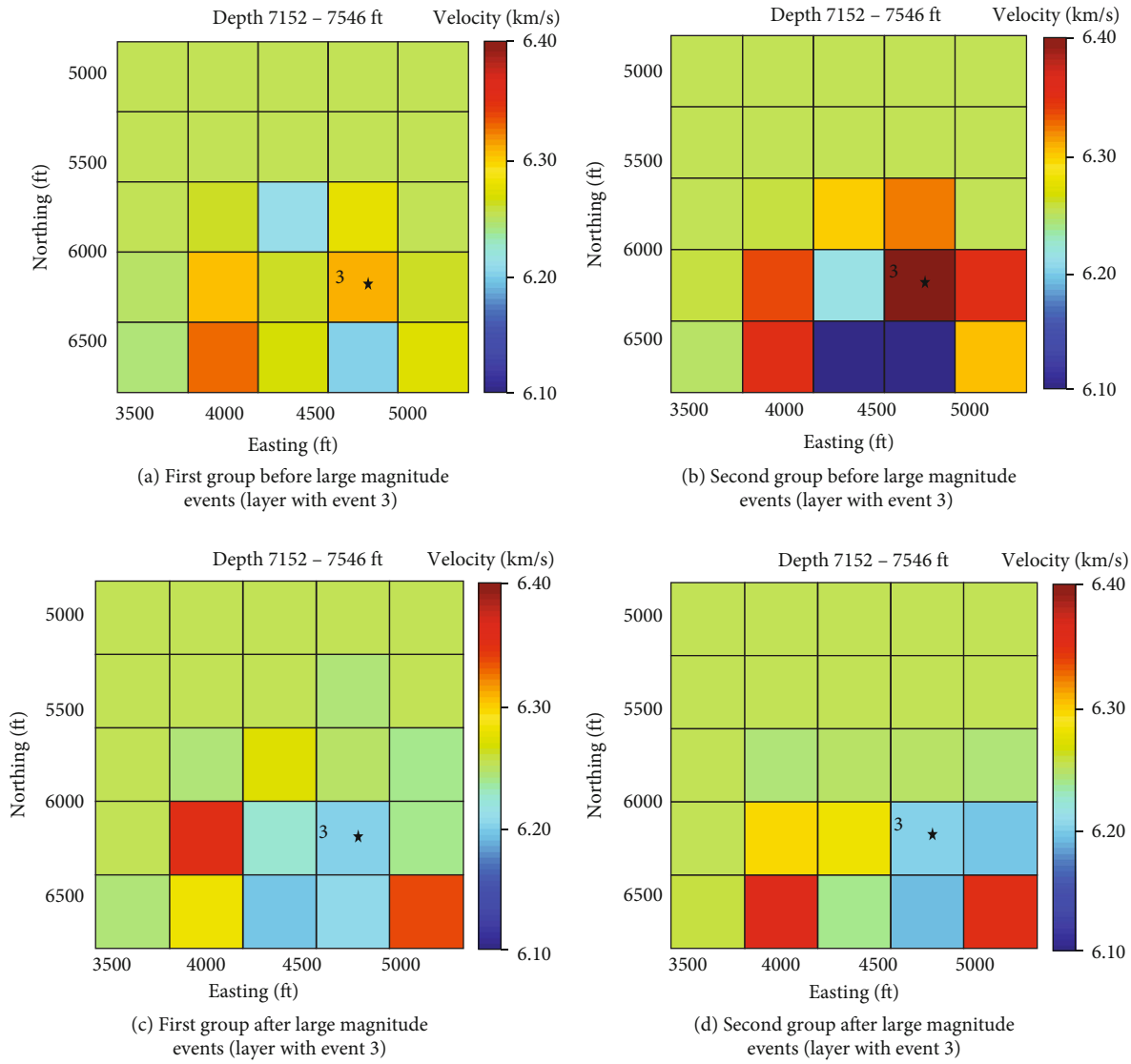

FIGURE 8: Temporal velocity evolution with mainshocks of Creighton Mine in depth range 2180-2300 m: (a) the first group (June 29 – July 1) before mainshocks; (b) the second group (July 1 – July 6) before mainshocks; (c) the first group (July 10 – July 12) after mainshocks; (d) the second group (July 12 – July 19) after mainshocks.

the geometry of velocity model. Travel time measurement and locations of seismic events are combined using double difference tomographic inversion to compute updated velocity models and relocations of seismic events at each iteration by LSQR algorithm [3, 4]. The conversion of the velocity models is validated by quantifying the residual of each iteration in the inversion. It is indicated that the residuals of travel time estimation keep decreasing with more iterations and converge after a series of iterations for tomographical studies of both Creighton Mine and Kidd Mine (Figure 6). The residual of Creighton Mine was smaller than that of Kidd Mine in average because the events quantity of every group of Creighton Mine is large than Kidd Mine. This proved that a better raypath coverage can decrease the residual of the inversions. More accurate velocity distributions are generated interacting with ultimate relocations of seismic events.

3. Results and Discussion

We examined the evolution of stress distribution by referring from the temporal velocity anomalies distribution using tomographic studies on historical seismicity data from two mines. The results of Creighton Mine and Kidd Mine are interpreted as follows.

3.1. Creighton Mine. Results of velocity distribution for mesh grids are exhibited in Figures 7 and 8. In Creighton Mine, Events 1, 2 and 4 are located in cubes on the level that ranges from 7546 ft (2300 m) to 7940 ft (2420 m) (Figure 7). Event 3 is located in cubes on the level ranges from 7152 ft (2180 m) to 7546 ft (2300 m) (Figure 8). The most conspicuous feature is that significant velocity changes around the mainshocks.

It is observed in Figure 7 that the velocities within the objective region surrounding Event 1, Event 2 and Event 4

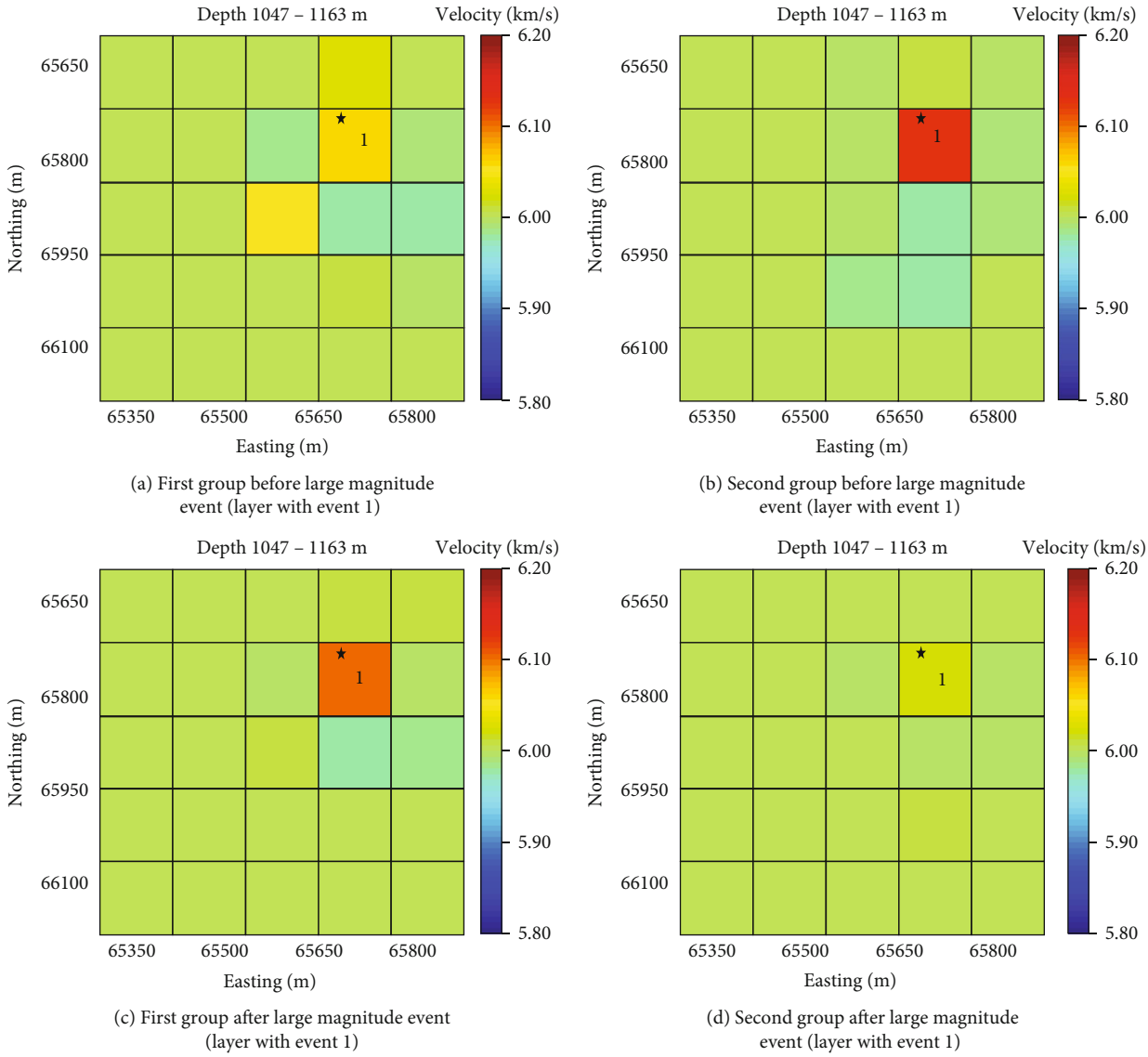

Figure 9: Temporal velocity evolution with mainshock 1 of Kidd Mine.

are higher than the background velocity for all the results from all event groups. High velocity anomalies are identified around Events 1, 2, and 4 before the mainshocks periods and the velocity increases significantly with the closer period to the occurrence of mainshocks (Figures 7(a) and 7(b)). However, velocity trend changes along with the occurrence of mainshocks. The velocity of the tabulation area especially including high velocities with events 1, 2 and 4 experienced a pronounced drop of velocity in the postseismic periods (Figures 7(b) and 7(c)). Eventually, the area with events 1, 2 and 4 continues to decrease to the level of background velocity. In addition to the fact that the region with events 1, 2, and 4 indicates the most striking velocity change, increasing before the seismic periods and decreasing in the coseismic and postseismic periods, other adjacent areas experienced similar velocity changes and reaches low velocities as well. Similarly, a significant velocity rising is manifested in the vicinity of Event 3 before the period ranges of large moment magnitude (Figures 8(a) and 8(b)). The region including Event 3 is identified by reductions in average wave speed comparing the velocity distribution before the mainshocks with that after the mainshocks, forming a slow velocity anomaly (Figures 8(b) and 8(c)). Two possible causes, including static stresses concentration and shaking damage, could be responsible for the velocity change. Static stress change can explain why the velocity anomalies are located nearby the mainshocks. The areas with static stress concentration are likely to cause the mainshocks. The high velocity areas before mainshocks suggest that a rock mass might be compacted due to the load force. A rock mass with a greater density is easier for waveform propagation. The most likely explanation for the vicinity of mainshocks appearing close to high velocity anomalies is that stress concentration enhances density of the rock mass. Bulk modulus of a rock mass is capable of increasing with volume decrease under the pressure. Volumetric hardening is likely to be invoked

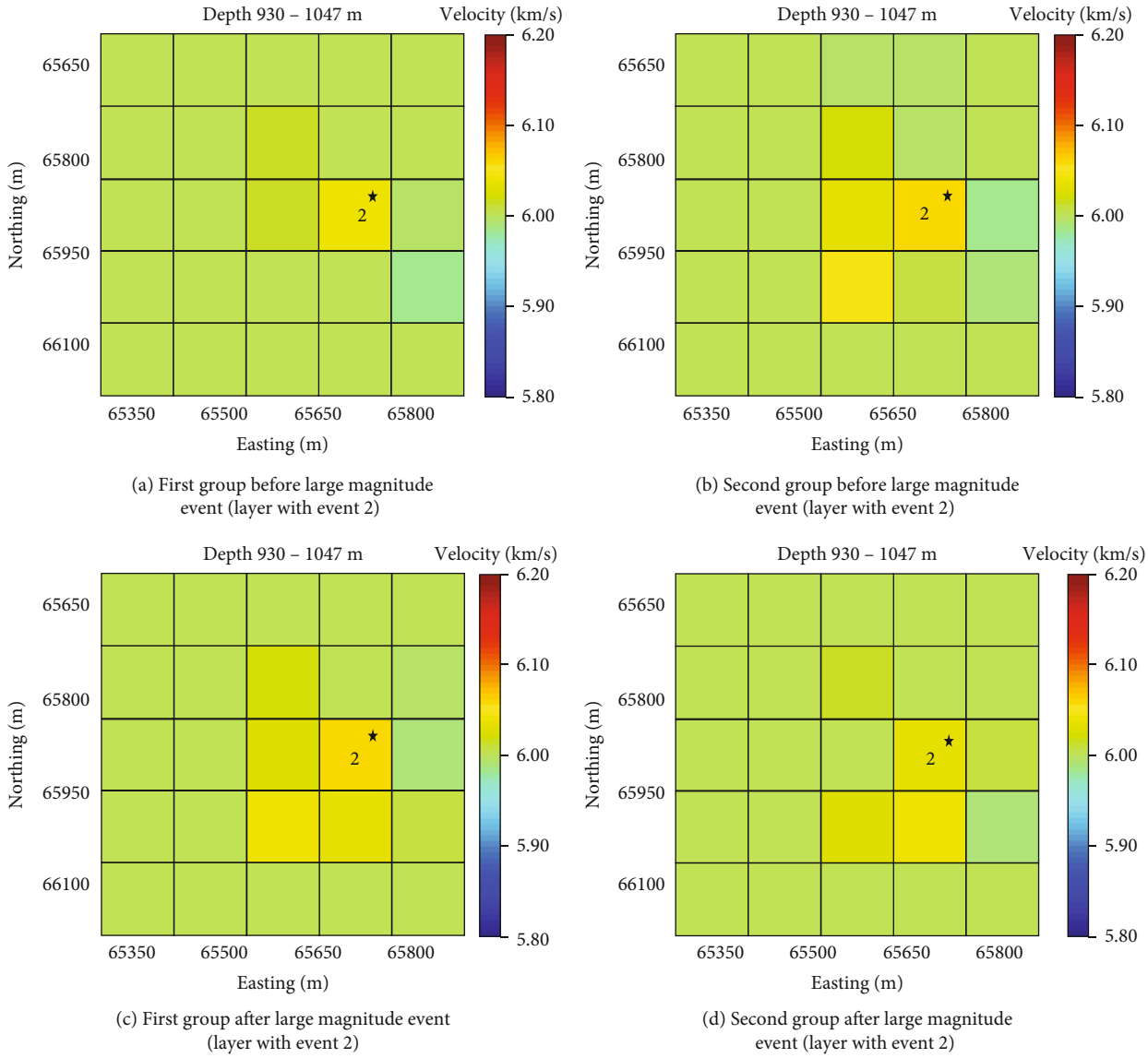

Figure 10: Temporal velocity evolution with mainshock 2 of Kidd Mine.

if the isotropic pressure causes irreversible volumetric compaction. Production blast activities are performed before the occurrence of mainshocks. It is inferred that production blast activities cause static stress change. As a result of static stress change, the stress field fails to keep the originally balanced state. Static stress change leads to uneven distribution in some regions. Abrupt energy release might be triggered to form the source of mainshocks.

After the mainshocks, velocities in the vicinity of mainshocks experienced a significant reduction associated with decreasing in varying extent of the other areas. A reasonable explanation is that the shaking effect by the mainshocks leads to ruptures and damage in nearby regions of rock mass. Opening of fractures by the shaking-induced damage impedes the propagation of waveform in rock mass. Shaking-induced damage is inversely correlated with the distance between its location and the hypocenter of mainshocks. This explains why the velocity drop is more evident on the regions that are closer to the location of mainshocks. The velocity around Event 3 changed more evidently than the region of the mainshock 1, 2, and 4 during the whole process. The coexistence of stress concentration and stress relaxation in a larger spatial scale implies that energy distribution tends to be in an overall equilibrium state. The region including Event 3 especially achieves a low velocity level right after the mainshocks in postseismic period.

3.2. Kidd Mine. According to the mainshocks of Kidd Mine, events group before and after the first mainshock (Event 1) and the second mainshock (Event 2) are analyzed, respectively. Analyses on microseismic events triggered before and after the seismic period in Kidd Mine are conducted to further illustrate the velocity change associated with the mainshocks. There is a strong similarity of velocity change pattern between Creighton Mine and Kidd Mine. It

demonstrates that velocity around Event 1 grows and forms a high velocity anomaly in the region before its occurrence (Figures 9(a) and 9(b).). It is inferred that the stress in the vicinity of mainshocks increases to a higher level and the waveform propagation of seismic events is strengthened before Event 1. The average velocity in the tabulation region of Event 1 also experiences a significant drop after Event 1 (Figures 9(b) and 9(c)). The average velocity of the region of Event 2 keeps higher than the background velocity (6.3 km/s) all the time. No pronounced velocity change is found in the region of Event 2. However, the total high velocity areas expand before the seismic period (Figures 10(a) and 10(b)) and then they diminish significantly in the postseismic periods (Figures 10(c) and 10(d).). It might be because the static stress is released and the propagation of dynamic shaking-induced fractures impair the waveform propagation after the occurrence of either Event 1 or Event 2.

The most noticeable difference between the velocity change with Event 1 and Event 2 is that the velocity change with Event 1 is strongly concentrated and is intense in comparison of the region of Event 2. The velocity changes with Event 2 are smoother and spread over larger areas. The reasonable explanation is that the magnitude of Event 1 is greater than the magnitude of Event 2. The hypothesis is that the dynamic-shaking induced effect from Event 1 is stronger than that from Event 2 is supported by the fact that the seismic energy of Event 1 is larger than Event 2.

4. Conclusions

This study investigated that the velocity of waveform propagation experienced changes within rock masses caused by mainshocks in underground mining. It is useful to have a simplified model that allows prediction of seismic risks in terms of mainshocks. Data sets from two hard rock underground mines are recorded and investigated. High seismic rates of each mine provide a good raypath coverage for objective regions. Groupings, comprised of one thousand events each, underwent velocity inversion in a double difference tomographic model to produce the velocity structures. In the comparison of velocity distribution of multiple periods close to mainshocks, some findings are summarized.

The waveform propagation is enhanced in the rockburst-prone (mainshocks) regions before their occurrence. It is inferred that high velocity anomalies are caused by the accumulation of static stress in the regions including potential mainshocks of the rock mass.

Velocity reduction after the mainshocks in the vicinity of them implies that static stress drop and dynamic-shaking induced fractures mutually lead to the weakness of waveform propagation. The rate and magnitude of velocity change seems related to the depth of occurrence and magnitude of events. It is found that P-wave velocity increased by 1% ~5% before the occurrence of mainshocks. After the mainshocks, the velocity turned into the state of decrease and eventually dropped to a level that was even lower than the average level before the occurrence of mainshocks. In the whole periods around the mainshocks, the difference between the lowest velocity and the highest velocity can be as high as 5%. It can be inferred that stress increased and formed a stress concentration region before the mainshocks. The occurrence of mainshocks caused damage and stress relaxation in the rock mass, leading to a significant velocity decrease.

Double-difference tomographic studies benefit the development of seismic hazard assessment in underground mining. The results presented in this study indicate that velocity anomalies within rock mass in underground mining are associated with the occurrence of mainshocks. It is possible to predict the mainshocks by detecting whether the wave speed changes in a relatively large amplitude compared with the historical data set. To explore the application of passive tomographic studies for seismic hazard assessment, tomographic investigation on microseismic data set during a long-term period would be attempted to accurately compute the ranges of velocity anomalies. Crucial thresholds of secure average velocity for a mine can be derived from multiple data sets of mining-induced seismicity. Seismic hazards in terms of mainshocks can be alerted when a velocity anomaly exceeds the threshold of secular velocity to improve the safety of underground mines.

Data Availability

The data can be available upon request.

Additional Points

Highlights. (i) Perform double-difference tomographic inversion to monitoring the velocity evolution of regions around mainshocks. (ii) Use tabular mesh grids to calculate the average velocity within specific time periods. (iii) Infer stress redistribution before and after the occurrence of mainshocks.

Conflicts of Interest

The authors have no conflicts of interest to declare that are relevant to the content of this article.

Acknowledgments

The author Xu Ma acknowledges the China National Key Research and Development Program (Grant no.: 2021YFC3000603). Support for this project came from a NIOSH Ground Control Capacity Building Grant (Contract 200-2011-40313). The author Kai Guo acknowledges the support from Science for Earthquake Resilience (Grant no. XH223706YB). The author Tao Yang is supported by the National Natural Science Foundation for Young Scientists of China (51974127). The author Enji Sun is supported by the National Key Research and Development Program of China (Grant no. 2017YFC0805100 and 2016YFC0801300).

References

[1] J. Korenaga, W. Holbrook, G. Kent et al., "Crustal structure of the Southeast Greenland margin from joint refraction and reflection seismic tomography," *Journal of Geophysical*

Research: Solid Earth (1978–2012), vol. 105, no. B9, pp. 21591–21614, 2000.

[2] C. Tape, Q. Liu, A. Maggi, and J. Tromp, "Seismic tomography of the southern California crust based on spectral-element and adjoint methods," *Geophysical Journal International*, vol. 180, no. 1, pp. 433–462, 2010.

[3] H. Zhang and C. Thurber, *User's manual for tomoDD1. 1 (double-difference tomography) For Determining Event Locations and Velocity Structure from Local Earthquakes and Explosions*, Department of Geology and Geophysics University of Wisconsin-Madison, Madison, WI, 2003.

[4] H. Zhang and C. H. Thurber, "Double-difference tomography: the method and its application to the Hayward fault, California," *Bulletin of the Seismological Society of America*, vol. 93, no. 5, pp. 1875–1889, 2003.

[5] D. P. Schaff and G. C. Beroza, "Coseismic and postseismic velocity changes measured by repeating earthquakes," *Journal of Geophysical Research: Solid Earth*, vol. 109, no. B10, 2004.

[6] D. A. Beck and B. H. G. Brady, "Evaluation and application of controlling parameters for seismic events in hard-rock mines," *International Journal of Rock Mechanics and Mining Sciences*, vol. 39, no. 5, pp. 633–642, 2002.

[7] Y.-G. Li, P. Chen, E. S. Cochran, J. E. Vidale, and T. Burdette, "Seismic evidence for rock damage and healing on the San Andreas Fault associated with the 2004 M 6.0 Parkfield earthquake," *Bulletin of the Seismological Society of America*, vol. 96, no. 4B, pp. S349–S363, 2006.

[8] Y.-G. Li, J. E. Vidale, S. M. Day, D. D. Oglesby, and E. Cochran, "Postseismic fault healing on the rupture zone of the 1999 M 7.1 Hector mine, California, earthquake," *Bulletin of the Seismological Society of America*, vol. 93, no. 2, pp. 854–869, 2003.

[9] M. Hudyma and Y. H. Potvin, "An engineering approach to seismic risk Management in Hardrock Mines," *Rock Mechanics and Rock Engineering*, vol. 43, no. 6, pp. 891–906, 2010.

[10] X. Ma, E. Westman, F. Malek, and M. Yao, "Stress redistribution monitoring using passive seismic tomography at a deep nickel mine," *Rock Mechanics and Rock Engineering*, vol. 52, no. 10, pp. 3909–3919, 2019.

[11] A. McGarr and R. Green, "Measurement of tilt in a deep-level gold mine and its relationship to mining and seismicity," *Geophysical Journal International.*, vol. 43, no. 2, pp. 327–345, 1975.

[12] T. Urbancic, C. Trifu, and R. Young, "Microseismicity derived fault-planes and their relationship to focal mechanism, stress inversion, and geologic data," *Geophysical Research Letters*, vol. 20, no. 22, pp. 2475–2478, 1993.

[13] E. C. Westman, R. J. Molka, and W. J. Conrad, "Ground control monitoring of retreat room-and-pillar mine in Central Appalachia," *International Journal of Mining Science and Technology*, vol. 27, no. 1, pp. 65–69, 2017.

[14] R. Young and S. Maxwell, "Seismic characterization of a highly stressed rock mass using tomographic imaging and induced seismicity," *Journal of Geophysical Research: Solid Earth (1978–2012)*, vol. 97, no. B9, pp. 12361–12373, 1992.

[15] W. G. Pariseau, M. K. McCarter, and J. M. Wempen, "Comparison of closure measurements with finite element model results in an underground coal mine in Central Utah," *International Journal of Mining Science and Technology*, vol. 29, no. 1, pp. 9–15, 2019.

[16] J. M. Wempen and M. K. McCarter, "Comparison of L-band and X-band differential interferometric synthetic aperture radar for mine subsidence monitoring in Central Utah," *International Journal of Mining Science and Technology*, vol. 27, no. 1, pp. 159–163, 2017.

[17] P. Konicek, J. Schreiber, and L. Nazarova, "Volumetric changes in the focal areas of seismic events corresponding to destress blasting," *International Journal of Mining Science and Technology*, vol. 29, no. 4, pp. 541–547, 2019.

[18] T. I. Urbancic and C. I. Trifu, "Recent advances in seismic monitoring technology at Canadian mines," *Journal of Applied Geophysics*, vol. 45, no. 4, pp. 225–237, 2000.

[19] J. Wesseloo, "The spatial assessment of the current seismic Hazard state for hard rock underground mines," *Rock Mechanics and Rock Engineering*, vol. 51, no. 6, pp. 1839–1862, 2018.

[20] M. A. Van Dyke, W. H. Su, and J. Wickline, "Evaluation of seismic potential in a longwall mine with massive sandstone roof under deep overburden," *International Journal of Mining Science and Technology*, vol. 28, no. 1, pp. 115–119, 2018.

[21] X. Ma, E. C. Westman, B. P. Fahrman, and D. Thibodeau, "Imaging of temporal stress redistribution due to triggered seismicity at a deep nickel mine," *Geomechanics for Energy and the Environment*, vol. 5, pp. 55–64, 2016.

[22] D. Malan and J. Napier, "A limit equilibrium fracture zone model to investigate seismicity in coal mines," *International Journal of Mining Science and Technology*, vol. 28, no. 5, pp. 745–753, 2018.

[23] A. Wuestefeld, J. M. Kendall, J. P. Verdon, and A. van As, "In situ monitoring of rock fracturing using shear wave splitting analysis: an example from a mining setting," *Geophysical Journal International*, vol. 187, no. 2, pp. 848–860, 2011.

[24] D. J. Holcomb, "Memory, relaxation, and microfracturing in dilatant rock," *Journal of Geophysical Research: Solid Earth*, vol. 86, no. B7, pp. 6235–6248, 1981.

[25] G. Mavko, T. Mukerji, and J. Dvorkin, *The Rock Physics Handbook : Tools for Seismic Analysis of Porous Media*, Cambridge University Press, 2010.

[26] F. Waldhauser and W. L. Ellsworth, "A double-difference earthquake location algorithm: method and application to the northern Hayward fault, California," *Bulletin of the Seismological Society of America*, vol. 90, no. 6, pp. 1353–1368, 2000.

[27] P. E. Share, H. Guo, C. H. Thurber, H. Zhang, and Y. Ben-Zion, "Seismic imaging of the southern California plate boundary around the south-central transverse ranges using double-difference tomography," *Pure and Applied Geophysics*, vol. 176, no. 3, pp. 1117–1143, 2019.